

Demographic-aware fine-grained classification of pediatric wrist fractures

Ammar Ahmed*, Ali Shariq Imran*, Zenun Kastrati†, Sher Muhammad Daudpota‡

*Department of Computer Science (IDI), Norwegian University of Science & Technology (NTNU), Gjøvik, 2815, Norway

†Department of Informatics, Linnaeus University, Växjö, 351 95, Sweden

‡Department of Computer Science, Sukkur IBA University, Sukkur, 65200, Pakistan

Abstract—Wrist pathologies are frequently observed, particularly among children who constitute the majority of fracture cases. However, diagnosing these conditions is time-consuming and requires specialized expertise. Computer vision presents a promising avenue, contingent upon the availability of extensive datasets, a notable challenge in medical imaging. Therefore, reliance solely on one modality, such as images, proves inadequate, especially in an era of diverse and plentiful data types. In this study, we employ a multifaceted approach to address the challenge of recognizing wrist pathologies using an extremely limited dataset. Initially, we approach the problem as a fine-grained recognition task, aiming to identify subtle X-ray pathologies that conventional CNNs overlook. Secondly, we enhance network performance by fusing patient metadata with X-ray images. Thirdly, rather than pre-training on a coarse-grained dataset like ImageNet, we utilize weights trained on a fine-grained dataset. While metadata integration has been used in other medical domains, this is a novel application for wrist pathologies. Our results show that a fine-grained strategy and metadata integration improve diagnostic accuracy by 2% with a limited dataset and by over 10% with a larger fracture-focused dataset.

Index Terms—Pediatric fracture classification, fracture detection, medical X-ray imaging, fine-grained classification, Patient metadata, multimodal

I. INTRODUCTION

Hand injuries are commonly seen in emergency departments, with wrist injuries being the most frequent. Distal radius and ulna fractures make up 75% of these wrist injuries [1]. Given the hand’s complex range of motion and functional importance, precise diagnosis and treatment are essential to prevent long-term functional impairment and disability. Recent advances in computer vision algorithms have shown potential in detecting trauma-related X-ray pathologies; however, these algorithms typically require large datasets for generalization, which is a challenge due to the limited availability of medical image datasets. Thus, combining additional data types with images can improve neural network learning. For example, incorporating patient demographic data with images has enhanced performance in skin cancer detection in various studies over the years [2]–[6].

However, there is a lack of investigation on integrating demographic data with X-ray images for wrist pathology classification. Data from the National Electronic Injury Surveillance System (NEISS) in the United States (1998–2013) indicates that the average age of pediatric patients with wrist fractures

is 10.9 years, with a gender distribution of 36% female and 64% male [7]. Studies show that 30–40% of girls and 40–50% of boys experience at least one fracture during childhood, with the wrist being the most frequently injured area [8], [9]. Among the 10–17 age group, males have a higher incidence of wrist fractures, with peak incidence at ages 13–14 for boys and 11–12 for girls, and a male-to-female ratio of 1.5. These findings demonstrate the correlation between age, gender, and fracture occurrence. We believe that by integrating these demographic factors, such as the age and gender of patients, with wrist X-rays, neural networks can achieve more accurate diagnostic decisions.

Many studies that combine patient metadata with visual data [2]–[6] utilize traditional CNN architectures such as ResNets, DenseNets, VGG, or Inception. These architectures, however, may not be ideal for detecting extremely small wrist pathologies in similar-looking wrist X-rays, making it harder for them to distinguish between pathologies accurately. To address this, we frame wrist pathology recognition as a fine-grained visual recognition (FGVR) problem, given the subtle and detailed nature of these conditions, as demonstrated in our previous work [10], [11]. We hypothesize that this approach, augmented by the fusion of demographic patient metadata and the refined architecture for joint learning introduced in this study, will outperform the baseline image-only method and several other widely used CNN architectures on this specific set of classes with a limited number of instances.

The goal of FGVR is to classify visually similar categories without needing manual annotation and extensive data, typically required by traditional CNN approaches. FGVR problems encounter two primary challenges. Firstly, there is substantial intra-class variance, as instances within the same class can be captured from diverse angles and perspectives. For instance, wrist fractures can appear differently in posteroanterior and lateral views within the fracture class. Secondly, subtle inter-class differences make distinguishing between classes difficult. For instance, it can be hard to tell apart conditions like fractures, bone anomalies, and soft tissue issues.

In this study, we utilize a transformer-based FGVR architecture adapted for incorporating various metadata types for joint learning. We curated two datasets: a smaller set with three wrist pathologies and a larger one, comparing fractures and non-fractures to demonstrate the effectiveness of the FGVR

approach paired with metadata fusion. First, it is demonstrated that the FGVR approach outperforms traditional and well-known image-only methods. Second, we integrate age and gender data with images within the FGVR architecture to show improvement in the performance. Third, to improve the performance even further, we pre-train the architecture on a fine-grained dataset, rather than on ImageNet. To the best of our knowledge, this study is the first to explore fine-grained classification combined with metadata integration on real-world X-rays of various projections and multiple wrist pathologies.

II. RELATED WORK

Most studies incorporating patient metadata with medical images have concentrated on skin lesion classification, leaving wrist pathologies largely unexplored. However, the demonstrated benefits of using patient metadata to improve performance provide valuable insights that can be applied to a range of medical fields. Thomas et al. [6] integrated images with metadata (age, gender, anatomical site) from the ISIC HAM10000 dataset using AlexNet, DenseNet201, ResNet50, Inception-resnetv2, VGG16, and GoogleNet. The integration of metadata improved the performance of all networks except for a slight degradation in VGG16.

Li et al. [5] integrated age, gender, and location with dermoscopy images from the ISIC 2018 dataset using AlexNet, ResNet, DenseNet, VGG, SENet, and PNASNet. Metadata fusion enhanced their PNASNet-based model, achieving an accuracy of 89.09%. Pacheco et al. [12] used custom patient skin cancer data. They employed MobileNet, VGGNet, GoogleNet, and ResNets, integrating patient metadata with images through a proposed aggregation mechanism, which improved balanced accuracy by approximately 7%. Nunnari et al. [3] used the ISIC 2019 dataset to classify skin lesions, integrating pixel data with age, gender, and body location. With VGG16 and ResNet50 as baselines, the shallow neural networks outperformed SVM and tree-based algorithms, achieving an accuracy of 83.34%. Age was identified as the most informative metadata feature.

Ningrum et al. [2] developed a method combining an ANN, which processed age, gender, anatomical site, and location, with a CNN to classify malignant and non-malignant melanomas in 23,801 dermoscopic images. Their approach achieved 92.34% accuracy, outperforming a standalone CNN. Pacheco et al. [13] used a MetaBlock to leverage metadata for classifying skin lesions, achieving mean accuracies of 80.7% (std 0.008) on ISIC 2019 and 74.8% (std 0.018) on PAD-UFES-20. Gessert et al. [14] combined EfficientNets, SENet, and ResNeXt-WSL models with metadata (age, sex, anatomical site), improving sensitivity, especially in smaller models, with a mean sensitivity of 74.2% (std 1.1) on ISIC 2019. Cai et al. [4] used ViT for image features and a Soft Label Encoder for metadata, achieving 93.81% accuracy on ISIC 2018 with age and location metadata.

These investigations consistently incorporate age and gender metadata, demonstrating an overall enhancement in per-

formance. This underscores the importance of demographic attributes in medical contexts. Given the absence of similar analyses for wrist pathologies, we draw inspiration from prior studies to evaluate the impact of demographic inclusion alongside image data in wrist pathology classification.

III. MATERIAL & METHODS

A. Dataset Curation

We curated a specialized dataset from the GRAZPEDWRI-DX dataset [15], designed for object detection, focusing on pediatric wrist radiography. This dataset includes 20,327 wrist images in PNG format from 6,091 patients, covering both lateral and posteroanterior projections, and featuring nine distinct abnormalities. Most instances belonged to the “fracture” class. Because some images contain multiple pathologies (e.g., two conditions in a single X-ray), we restricted our dataset to images exhibiting only a single class for multi-class recognition. This decision reflects a common constraint in real-world medical datasets, which typically lack annotated bounding boxes and rely instead on image-level annotations. This single-pathology per image extraction resulted in a dataset with significant class imbalance.

To address this, we excluded classes with fewer than 100 instances to avoid redundancy post-augmentation. Furthermore, we exclude the “metal” class, as our focus is on inherent wrist pathologies rather than the presence of external objects visible in the radiographs. Hence, from the original nine classes, three were selected for this study: Boneanomaly (87 instances), Fracture (10,026 instances), and Softtissue (117 instances).

For training and testing, 20% of the data from each class, except “fracture” was reserved for testing, with the rest used for training. For testing purposes, we augment the existing images in the test set to achieve approximately 120 images per class and downsample the “fracture” class to 120 instances. Regarding the training set, we used 500 “fracture” instances and augmented the remaining two classes. This set was then further split into 80% for training and 20% for validation.

The number of instances in the final split for the limited set (Three Wrist Pathologies) is shown in the left sub-table of Table I. In addition, we also curated an additional dataset containing all images from the dataset. To achieve this, we categorized the dataset into two classes: “Fracture” and “No Fracture”. This would then serve to further evaluate the influence of metadata integration when utilizing the entire dataset. The distribution of training, validation, and test sets for this dataset is also detailed in Table I. In this case, the “No Fracture” class was augmented to approximate the number of instances in the “fracture” class. The final split ratio is 86.65% for training, 10.68% for validation, and 2.66% for testing.

B. Metadata Analysis

The dataset includes patients with an average age of 10.9 years, ranging from 0.2 to 19 years. It comprises 2,688 female patients, 3,402 male patients, and one patient with unrecorded gender information. Patient metadata is derived from the filename structure of each image, as shown in Figure 1.

TABLE I: Number of Instances in Training, Validation, and Test Sets

Three Wrist Pathologies (Limited set)				Fracture vs. No Fracture (Entire set)			
Class	Training	Validation	Test	Class	Training	Validation	Test
Boneanomaly	392	98	119	Fracture	11854	1357	338
Fracture	400	100	120	No Fracture	10164	1357	338
Soft-tissue	376	94	115				
Total	1168	292	354	Total	22018	2714	676

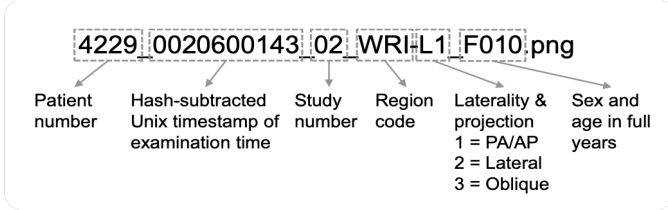


Fig. 1: Filename structure of GRAZPEDWRI-DX dataset [15].

A bar plot illustrating the distribution of fractures and no-fracture cases among males and females is shown in Figure 2. It reveals a significantly higher incidence of fractures among males, with a larger proportion of females not exhibiting fractures compared to males. This distribution is consistent across other pathologies as well. The box plot for fractures shows that 50% of males fall between approximately 8 and 13 years old, with the remaining 25% below 8 years and 25% above 13 years. Females with fractures typically range between about 7.5 and 11 years old, with a maximum of just below 17.5 years for females and slightly above 18 years for males. For individuals without fractures, 75% of females are older than 9 years, and 75% of males are older than approximately 10 years. In the wrist pathology dataset, males with bone anomalies are typically aged between about 13.5 and just below 17.5 years, while females range from approximately 11 to 13.5 years. For soft tissue pathology, males are aged between 11 and 15 years, and females between about 9 and just below 15 years, with a minimum age of around 2.5 years for females and around 7.5 years for males.

C. Architectural Details

This work utilizes a hybrid architecture that integrates both visual data and meta-information, drawing inspiration from the architecture called “MetaFormer” [16]. The approach builds on the Vision Transformer framework, treating images as sequences of patch tokens, but extends it by introducing additional tokens that encode supplementary metadata. This fusion allows for more nuanced, fine-grained visual recognition by combining the local feature extraction strength of convolutions with the global context modeling capabilities of transformers.

As depicted in Figure 3, the architecture is organized into five stages. The first stage (S0) starts with a basic 3-layer convolutional stem, which processes raw input images. Subsequent stages progressively downsample the feature maps and increase channel dimensionality. Stages S1 and S2 consist of Mobile Inverted Bottleneck Convolution (MBCConv) blocks enhanced with squeeze-and-excitation mechanisms. The final

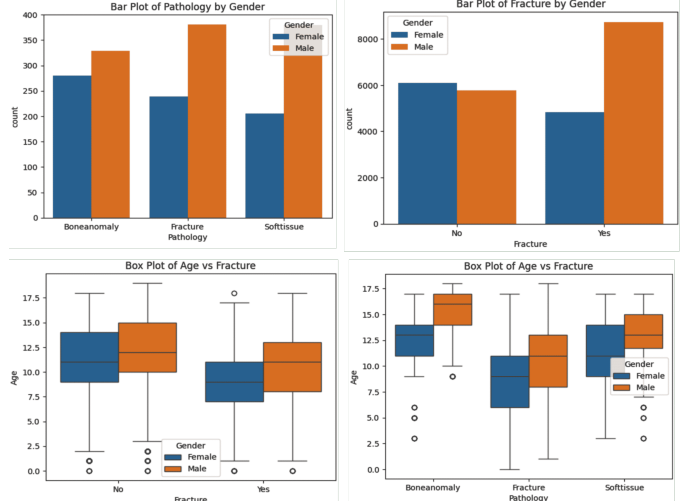


Fig. 2: Bar and box plots for gender and age, respectively, for both curated datasets.

TABLE II: Configuration of the architecture series. B represents the number of blocks, and H denotes the hidden dimensions for each stage.

Stage	FG-0	FG-1	FG-2
S0	B=3 H=64	B=3 H=64	B=3 H=128
S1	B=2 H=96	B=2 H=96	B=2 H=128
S2	B=3 H=192	B=6 H=192	B=6 H=256
S3	B=5 H=384	B=14 H=384	B=14 H=512
S4	B=2 H=768	B=3 H=768	B=3 H=1024

two stages, S3 and S4, transition to transformer-based blocks that employ relative positional encoding.

Downsampling is applied at the beginning of each stage. In S3 and S4, overlapping patch embedding is implemented using convolutions with a stride of 2 and zero-padding, effectively reducing resolution while maintaining contextual overlap [17]. Table II outlines the configuration details of the three variants of the architecture used in our experiments.

To overcome the lack of spatial awareness in standard self-attention, the model incorporates a relative position bias. Specifically, a bias matrix $B \in \mathbb{R}^{((M^2+N) \times (M^2+N))}$ is added during attention computation:

$$Attention(Q, K, V) = \text{Softmax} \left(\frac{QK^T}{\sqrt{d}} + B \right) V \quad (1)$$

Here, Q , K , and V are the query, key, and value matrices of size $\mathbb{R}^{((M^2+N) \times d)}$, where M^2 corresponds to the number of image patches and N is the count of extra tokens (e.g.,

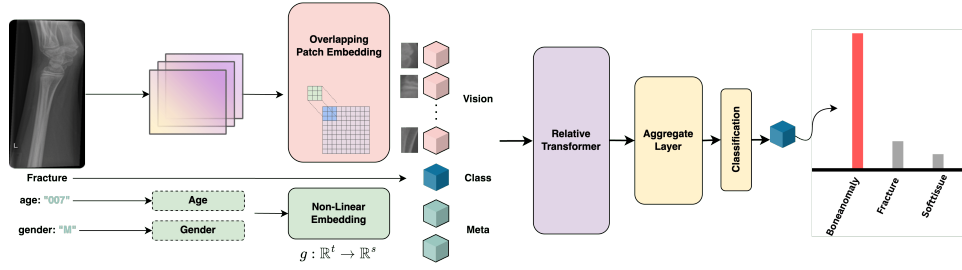


Fig. 3: The architecture integrates visual, class, and meta tokens within a transformer framework. Meta-information is embedded using a non-linear projection. Fusion occurs through a Relative Transformer Layer, and classification is performed using the final class token.

class and meta tokens). The bias matrix \hat{B} is parameterized as described in [18], supporting relative positions from $-M - 1$ to $M + 1$. A shared bias is applied for non-visual tokens since their spatial position is undefined.

The Relative Transformer Block comprises multi-head self-attention (MSA), layer normalization (LN), and a multi-layer perceptron (MLP), applied to the input token sequence z_0 :

$$\begin{aligned} z_0 &= [x_{\text{class}}; x_{\text{meta}}^1, \dots, x_{\text{meta}}^{n-1}; x_{\text{vision}}^1, \dots, x_{\text{vision}}^m] \\ z'_i &= \text{MSA}(\text{LN}(z_{i-1})) + z_i \\ z_i &= \text{MLP}(\text{LN}(z'_i)) + z'_i \end{aligned} \quad (2)$$

In this formulation, $z_i \in \mathbb{R}^{(M^2+N) \times d}$ captures the updated token sequence at each transformer layer.

Stages S3 and S4 each generate a class token— z_{class}^1 and z_{class}^2 —which encode combined visual and meta representations. Since these tokens may differ in dimension, z_{class}^1 is first projected to match the shape of z_{class}^2 using an MLP. The two are then concatenated and passed through a 1D convolution followed by normalization:

$$\begin{aligned} \hat{z}_{\text{class}}^1 &= \text{MLP}(\text{LN}(z_{\text{class}}^1)) \\ z_{\text{class}} &= \text{Conv1d}(\text{Concat}(\hat{z}_{\text{class}}^1, z_{\text{class}}^2)) \\ y &= \text{LN}(z_{\text{class}}) \end{aligned} \quad (3)$$

The final output y aggregates information across multiple scales and token types. When using external attributes as metadata, these are encoded as vectors and embedded using a fully connected non-linear function $f: \mathbb{R}^n \rightarrow \mathbb{R}^d$. For instance, our curated dataset with two attribute values would produce a 2D input vector, which is then projected into the same embedding space as the vision tokens.

To maintain the model’s ability to learn important visual features, especially when metadata is less informative or potentially overfitting, a regularization strategy is applied during training that progressively masks parts of the meta-information. This balances the reliance on both vision and auxiliary data.

D. Experimental Settings

A range of well-established models has been incorporated in our study alongside our fine-grained metadata-aware ap-

TABLE III: Performance evaluation of different baseline neural networks and the MetaFormer on only image data.

Model	Test Accuracy (Vision Only)
ViT	62.71%
VGG16	63.28%
GoogleNet	70.34%
EfficientNetV2	72.32%
AlexNet	74.29%
DenseNet201	76.84%
InceptionV3	77.44%
ResNet50	77.68%
MetaFormer FGVR (Base)	79.40%

proach for comparison. All these baseline models were pre-trained on ImageNet [19]. These include ViT [20], VGG16 [21], GoogleNet [22], EfficientNetV2 [23], AlexNet [24], DenseNet201 [25], InceptionV3 [26], and ResNet50 [27]. All models underwent training for 100 epochs using an image resolution of 224x224 and a batch size of 32. Adam optimizer was utilized with a learning rate $\eta = 5 \times 10^{-3}$. For MetaFormer, however, the base learning rate was $\eta = 1 \times 10^{-4}$, warmup learning rate $\alpha = 5 \times 10^{-7}$, minimum learning rate was $\eta_m = 1 \times 10^{-5}$, and weight decay was $\wp = 5 \times 10^{-2}$.

For the augmentation procedure, prior to training, we utilized Keras’ ImageDataGenerator with the following parameters:

$$\begin{aligned} \text{rotation_range} &= 15, \\ \text{width_shift_range} &= 0.2, \\ \text{height_shift_range} &= 0.1, \\ \text{horizontal_flip} &= \text{True}, \\ \text{shear_range} &= 0.2, \\ \text{brightness_range} &= (0.7, 1.3), \\ \text{zoom_range} &= 0.1, \\ \text{fill_mode} &= \text{“constant”}, \\ \text{zca_whitening} &= \text{True}. \end{aligned}$$

Although the choice of these parameter values may seem arbitrary, we carefully selected them to strike a balance between enhancing the images effectively and avoiding excessive rotation, shifting, brightness alterations, or zooming that could cause images to be misaligned or overly exposed.

TABLE IV: Accuracy of different MetaFormer configurations on only image data, integrating metadata through early fusion, and integrating metadata through late fusion.

Model Configuration	Vision Only	Early Fusion	Late Fusion
FG-0	79.4%	79.1%	80.5%
FG-1	78.5%	80.5%	79.1%
FG-2	77.4%	78.5%	79.4%
FG-2-inat (Fine-grained pre-training)	79.9%	81.1%	81.4%

TABLE V: Evaluation of our configuration of MetaFormer(FG-2-inat) using sensitivity, specificity, and precision.

Configuration	Cls	Sensitivity	Specificity	Precision
Vision Only	0	62.2%	98.7%	96.1%
	1	100%	82.9%	75%
	2	77.4%	88.3%	76.1%
Vision+Meta	0	66.4%	98.7%	96.3%
	1	100%	82.9%	75%
	2	77.4%	90.4%	79.5%

TABLE VI: Table showing accuracies obtained by our configuration of MetaFormer on individual metadata attributes and when both attributes are considered.

Attribute	Early Fusion	Late Fusion
Vision + Age	80.5%	79.4%
Vision + Gender	79.9%	80.8%
Vision + Age + Gender	81.1%	81.4%

IV. RESULTS & DISCUSSION

To begin our discussion, we present the results from both baseline CNN models and MetaFormer for fine-grained recognition of wrist pathologies trained exclusively on image data. The test accuracies achieved by each neural network are summarized in Table III. The chosen baseline methods show lower accuracy compared to MetaFormer. It seems that the intricate nature of wrist pathologies allows MetaFormer to achieve relatively higher performance compared to other contemporary and commonly used baseline methods.

Having established MetaFormer’s superior performance over established CNN models trained solely on image data, we proceeded to integrate image and metadata (gender and age) for MetaFormer. Table IV shows the performance of various MetaFormer configurations: trained exclusively on image data, integrating metadata through early fusion, and integrating metadata through late fusion. It is evident that integrating metadata, whether through early or late fusion, outperformed configurations trained solely on image data. Additionally, late fusion demonstrated higher accuracy than early fusion in two of the three configurations, except for “FG-1” This advantage of late fusion could be due to several reasons. First, late fusion may be more robust to noise in individual modalities, as combining information at a later stage allows the final decision to benefit from multiple sources, potentially mitigating the impact of noise or errors in any single modality. Second, late fusion can help reduce overfitting.

But does that definitely confirm the hypothesis of whether metadata can improve classification performance in conjunction with image data? To further validate whether incorporat-

TABLE VII: Performance evaluation of AlexNet with and without fusing vision with metadata.

Approach	Test Accuracy
Vision Only	74.29%
Vision + Meta	77.40%

TABLE VIII: Performance evaluation on significantly larger (fracture vs. no fracture) dataset.

Our MetaFormer Configuration	Test Accuracy
Vision Only	50.1%
Vision + Meta	60.4%

ing metadata helps in classification, we modified the AlexNet architecture and integrated metadata to see any improvements, the results of which can be seen in Table VII. It seems the metadata does help even if the architecture is much simpler.

We then selected the “FG-2” configuration from Table IV and used the fine-grained weights obtained from training MetaFormer on the iNaturalist dataset [28] to create the “FG-2-inat” configuration. This surpassed all other configurations, whether using image data alone or in conjunction with metadata. The highest accuracy achieved was 81.4%, a significant 1.5% improvement compared to using only vision information. It is evident that using pre-trained weights from a fine-grained dataset and transferring that knowledge to another fine-grained task yields significantly better results compared to using pre-trained weights from the coarse-grained ImageNet dataset. Additionally, when integrating metadata, the model reached its highest validation accuracy at the 80th epoch, with no further improvement in subsequent epochs.

In contrast, when using only vision, the model learned more slowly, achieving its highest validation accuracy at the 96th epoch. The confusion matrix generated by the configuration “FG-2-inat” using the late fusion strategy, shown in Figure 4, indicates a slight increase in correctly classified instances in the “boneanomaly” class, with one fewer correct classification in the “softtissue” class, while all “fracture” instances are accurately identified. Nevertheless, integrating age and gender metadata has positively impacted the system’s overall performance. Table V presents the sensitivity, specificity, and precision achieved by MetaFormer on vision-only and vision + metadata configurations. Notably, there is a 4.2% increase in sensitivity for the “boneanomaly” class and a 3.4% increase in precision for the “softtissue” class.

We individually trained our MetaFormer configuration on the metadata attributes of “age” and “gender” alongside vision to assess their respective contributions to enhancing network performance. As depicted in Table VI, both attributes

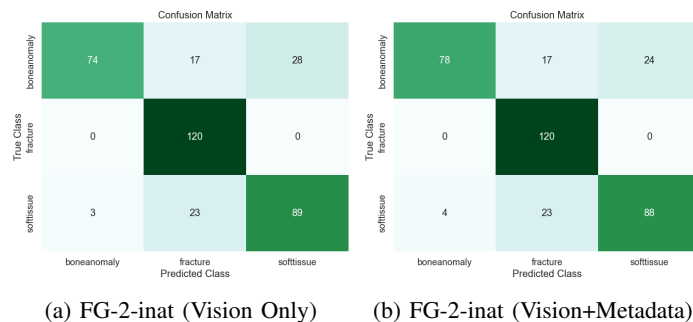


Fig. 4: Confusion matrices for FG-2-inat configuration.

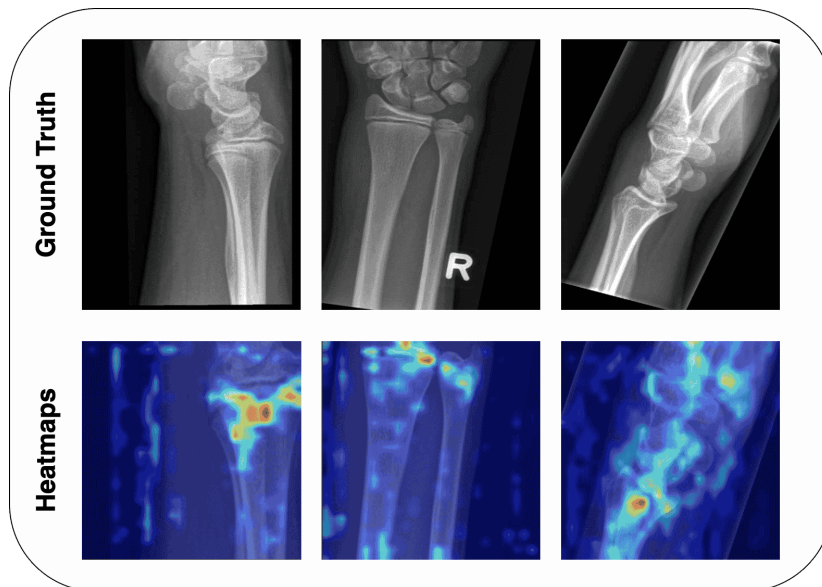


Fig. 5: Heatmaps generated from the final convolutional layer in stage 2 (S2) of our configuration fine-grained-FG-2 on a limited dataset. The areas of interest are highlighted with more intensity, particularly around the regions where pathologies are likely to be present.

yielded comparable results. The highest accuracy of 80.8% was achieved when the model was trained on “gender” using the late fusion strategy. Interestingly, the model’s inability to surpass the 81.4% accuracy achieved when both attributes were utilized supports the notion that both “age” and “gender” play crucial roles in enhancing performance.

To further evaluate the effects of combining image metadata with image features, we also trained the same MetaFormer configuration on the “Fracture vs. No Fracture” dataset, which contains significantly more samples than the limited dataset of wrist pathologies. As shown in Table VIII, integrating metadata with vision in the larger dataset increased the accuracy by 10 percent, a significant improvement. Conducting this experiment on the entire dataset, rather than a subset, revealed a substantial enhancement when including metadata alongside images, highlighting the importance of integrating metadata in wrist medical conditions.

Using our configuration of the network (Fine-grained-FG-2), we generated heatmaps using GradCAM [29] from the

last convolutional layer in stage 2 (S2), shown in Figure 5. The heatmaps indicate that our model is able to localize key features in the X-ray images. The areas of interest are highlighted with more intensity, particularly around the regions where pathologies are likely to be present. Given that the model was trained on extremely limited data, its ability to generate meaningful heatmaps that align well with the ground truth images suggests a strong capacity for generalization. This is an impressive feat, especially considering that conventional CNNs often struggle under similar constraints. The heatmaps demonstrate that the model is capturing fine-grained details in the X-rays.

However, the approach is not without its limitations. Some of the heatmaps show diffuse or less focused attention areas, indicating that the model may sometimes struggle to pinpoint the exact location of abnormalities. This could result in reduced diagnostic accuracy, particularly in more ambiguous cases where the model is uncertain. In a few instances, the heatmaps suggest that the model’s attention may be spread

across multiple areas that do not align perfectly with the abnormalities seen in the X-rays. This misalignment could imply that the model is capturing some irrelevant features or noise, which could lead to false positives or a less reliable diagnosis.

V. CONCLUSION & FUTURE WORK

In this study, we demonstrated that integrating patient demographic metadata with image data enhances fine-grained recognition of pediatric wrist fractures and other pathologies. Pre-training on a fine-grained dataset, rather than ImageNet, further improved performance across domains. These findings highlight the value of using patient demographic information for more accurate diagnoses. Future research should explore alternative fine-grained architectures and additional patient metadata to continue improving medical image analysis.

VI. ACKNOWLEDGEMENT

This work was supported by the Curricula Development and Capacity Building in Applied Computer Science for Pakistani Higher Education Institutions (CONNECT) Project NORPART-2021/10502, funded by the Norwegian Directorate for Higher Education and Skills (DIKU).

REFERENCES

- [1] B. C. M. Hoynak, "Wrist Fracture Management in the ED," *Practice Essentials, Pathophysiology, Prognosis, Medscape*, 2022.
- [2] D. N. A. Ningrum, S.-P. Yuan, W.-M. Kung, C.-C. Wu, I.-S. Tzeng, C.-Y. Huang, J. Y.-C. Li, and Y.-C. Wang, "Deep Learning Classifier with Patient's Metadata of Dermoscopic Images in Malignant Melanoma Detection," *Journal of Multidisciplinary Healthcare*, vol. 14, pp. 877–885, 2021.
- [3] F. Nunnari, C. Bhuvaneshwara, A. O. Ezema, and D. Sonntag, "A Study on the Fusion of Pixels and Patient Metadata in CNN-Based Classification of Skin Lesion Images," in *Machine Learning and Knowledge Extraction*, A. Holzinger, P. Kieseberg, A. M. Tjoa, and E. Weippl, Eds. Springer International Publishing, 2020, pp. 191–208.
- [4] G. Cai, Y. Zhu, Y. Wu, X. Jiang, J. Ye, and D. Yang, "A Multimodal Transformer to Fuse Images and Metadata for Skin Disease Classification," *The Visual Computer*, vol. 39, no. 7, pp. 2781–2793, 2023.
- [5] W. Li, J. Zhuang, R. Wang, J. Zhang, and W.-S. Zheng, "Fusing metadata and dermoscopy images for skin disease diagnosis. IEEE Conference Publication — IEEE Xplore.
- [6] S. A. Thomas, "Combining Image Features and Patient Metadata to Enhance Transfer Learning," in *2021 43rd Annual International Conference of the IEEE Engineering in Medicine and Biology Society (EMBC)*, 2021, pp. 2660–2663.
- [7] E. M. Z. Neil S Shah, David Buzas. (2015) Epidemiologic dynamics contributing to pediatric wrist fractures in the united states. Read by QxMD.
- [8] H. Südow and C. Mellstrand Navarro, "The Incidence of Distal Radius Fractures in a Swedish Pediatric Population - an Observational Cohort Study of 90 970 Individual Fractures," *BMC Musculoskeletal Disorders*, vol. 22, no. 1, p. 564, 2021.
- [9] E. M. Hedström, O. Svensson, U. Bergström, and P. Michno, "Epidemiology of Fractures in Children and Adolescents," *Acta Orthopaedica*, vol. 81, no. 1, pp. 148–153, 2010.
- [10] A. Ahmed, A. S. Imran, Z. Kastrati, S. M. Daudpota, M. Ullah, and W. Noor, "Learning from the few: Fine-grained approach to pediatric wrist pathology recognition on a limited dataset," *Computers in Biology and Medicine*, vol. 181, p. 109044, Oct 2024. [Online]. Available: <https://www.sciencedirect.com/science/article/pii/S0010482524011296>
- [11] A. Ahmed, A. S. Imran, M. Ullah, Z. Kastrati, and S. M. Daudpota, "Navigating limitations with precision: A fine-grained ensemble approach to wrist pathology recognition on a limited x-ray dataset," in *2024 IEEE International Conference on Image Processing (ICIP)*, 2024, pp. 3077–3083.
- [12] A. G. C. Pacheco and R. A. Krohling, "The Impact of Patient Clinical Information on Automated Skin Cancer Detection," *Computers in Biology and Medicine*, vol. 116, p. 103545, 2020.
- [13] A. G. C. Pacheco and R. A. Krohling, "An Attention-Based Mechanism to Combine Images and Metadata in Deep Learning Models Applied to Skin Cancer Classification," *IEEE Journal of Biomedical and Health Informatics*, vol. 25, no. 9, pp. 3554–3563, 2021.
- [14] N. Gessert, M. Nielsen, M. Shaikh, R. Werner, and A. Schlaefler, "Skin Lesion Classification Using Ensembles of Multi-Resolution EfficientNets with Meta Data," *MethodsX*, vol. 7, p. 100864, 2020.
- [15] E. Nagy, M. Janisch, F. Hrzić, E. Sorantin, and S. Tschauner, "A pediatric wrist trauma x-ray dataset (grazpedwri-dx) for machine learning," *Nature News*, 2022.
- [16] Q. Diao, Y. Jiang, B. Wen, J. Sun, and Z. Yuan, "MetaFormer: A Unified Meta Framework for Fine-Grained Recognition," *arXiv.org*, 2022.
- [17] W. Wang, E. Xie, X. Li, D.-P. Fan, K. Song, D. Liang, T. Lu, P. Luo, and L. Shao, "Pvtv2: Improved Baselines with Pyramid Vision Transformer," *arXiv preprint*, 2021.
- [18] Z. Liu, Y. Lin, Y. Cao, H. Hu, Y. Wei, Z. Zhang, S. Lin, and B. Guo, "Swin Transformer: Hierarchical Vision Transformer using Shifted Windows," *arXiv preprint*, 3 2021, arXiv:2103.14030.
- [19] J. Deng, W. Dong, R. Socher, L.-J. Li, K. Li, and L. Fei-Fei, "Imagenet: A large-scale hierarchical image database," in *Proceedings of the IEEE Conference on Computer Vision and Pattern Recognition (CVPR)*. IEEE, 2009, pp. 248–255. [Online]. Available: <https://ieeexplore.ieee.org/document/5206848>
- [20] A. Dosovitskiy, L. Beyer, A. Kolesnikov, D. Weissenborn, X. Zhai, T. Unterthiner, M. Dehghani, M. Minderer, G. Heigold, S. Gelly, J. Uszkoreit, and N. Houlsby, "An Image is Worth 16x16 Words: Transformers for Image Recognition at Scale," 2020.
- [21] K. Simonyan and A. Zisserman, "Very Deep Convolutional Networks for Large-Scale Image Recognition," 2015.
- [22] C. Szegedy, W. Liu, Y. Jia, P. Sermanet, S. Reed, D. Anguelov, D. Erhan, V. Vanhoucke, and A. Rabinovich, "Going deeper with convolutions," in *2015 IEEE Conference on Computer Vision and Pattern Recognition (CVPR)*. IEEE, 2015, pp. 1–9.
- [23] M. Tan and Q. V. Le, "EfficientNetV2: Smaller Models and Faster Training," 2021. [Online]. Available: <https://arxiv.org/abs/2104.00298>
- [24] A. Krizhevsky, I. Sutskever, and G. E. Hinton, "ImageNet Classification with Deep Convolutional Neural Networks," in *Advances in Neural Information Processing Systems*, 2012. [Online]. Available: <https://papers.nips.cc/paper/2012/hash/c399862d3b9d6b76c8436e924a68c45b-Abstract.html>
- [25] G. Huang, Z. Liu, L. van der Maaten, and K. Q. Weinberger, "Densely Connected Convolutional Networks," 2018. [Online]. Available: <https://arxiv.org/abs/1608.06993>
- [26] C. Szegedy, W. Liu, Y. Jia, P. Sermanet, S. Reed, D. Anguelov, D. Erhan, V. Vanhoucke, and A. Rabinovich, "Going Deeper with Convolutions," 2014.
- [27] K. He, X. Zhang, S. Ren, and J. Sun, "Deep Residual Learning for Image Recognition," 2015. [Online]. Available: <https://arxiv.org/abs/1512.03385>
- [28] G. Van Horn, O. Mac Aodha, Y. Song, Y. Cui, C. Sun, A. Shepard, H. Adam, P. Perona, and S. Belongie, "The iNaturalist Species Classification and Detection Dataset," *arXiv.org*, April 2018.
- [29] R. R. Selvaraju, M. Cogswell, A. Das, R. Vedantam, D. Parikh, and D. Batra, "Grad-cam: Visual explanations from deep networks via gradient-based localization," *International Journal of Computer Vision*, vol. 128, no. 2, pp. 336–359, 2019. [Online]. Available: <https://doi.org/10.1007/s11263-019-01228-7>